ARTICLE

Gas-phase synthesis of Ti$_2$CCl$_2$ enables an efficient catalyst for lithium-sulfur batteries
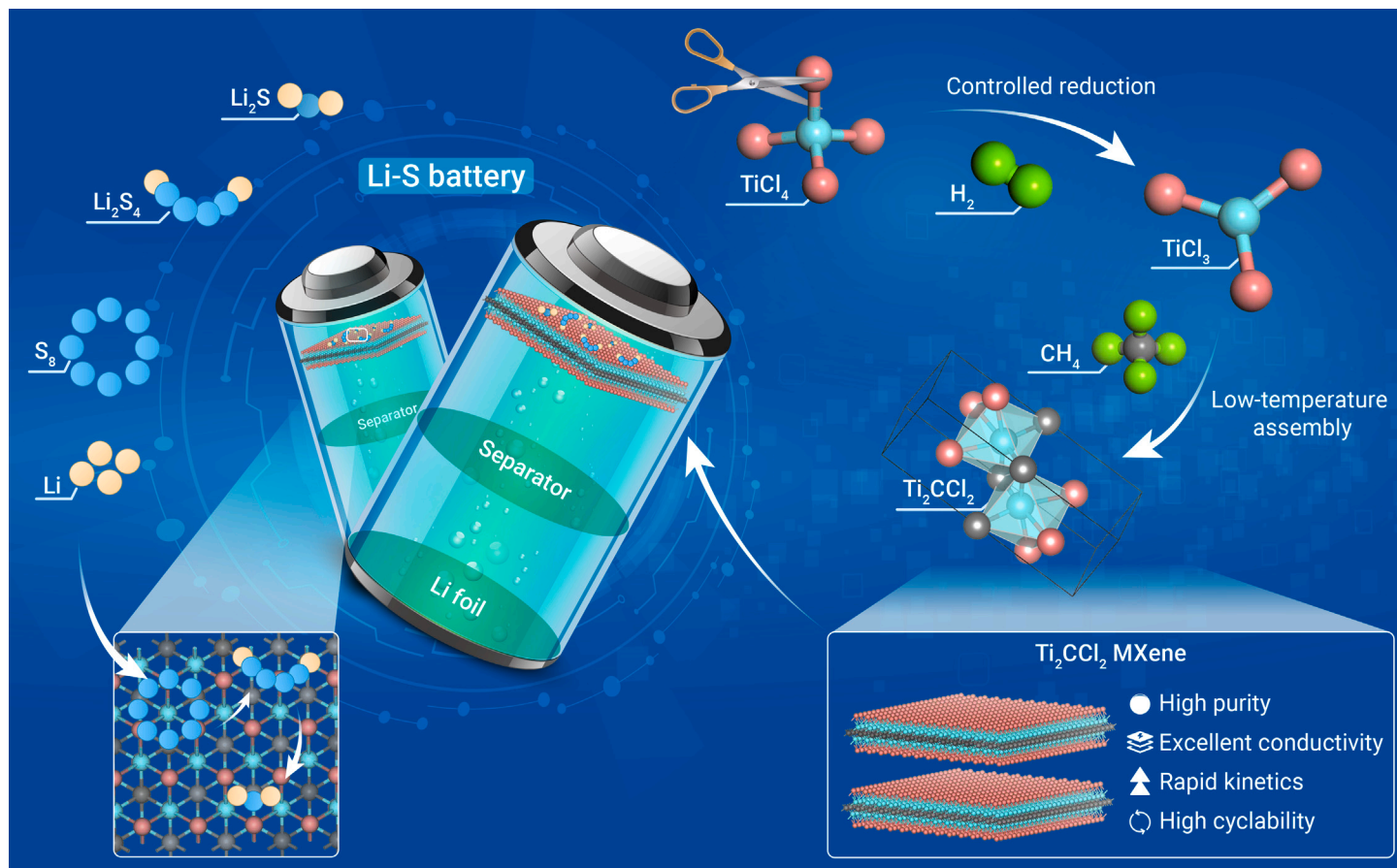
Maoqiao Xiang,[1,2] Zihan Shen,[1] Jie Zheng,[1,2] Miao Song,[1,4] Qiya He,[1] Yafeng Yang,[1,2] Jiuyi Zhu,[1] Yuqi Geng,[1,2] Fen Yue,[1,2] Qinghua Dong,[1,2] Yu Ge,[1] Rui Wang,[1,2] Jiake Wei,[6] Weiliang Wang,[7] Haiming Huang,[8] Huigang Zhang,[1,2,*] Qingshan Zhu,[1,2,3,*] and Chuanfang John Zhang[5]

*Correspondence: hgzhang@ipe.ac.cn (H.Z.); qszhu@ipe.ac.cn (Q.Z.)

GRAPHICAL ABSTRACT

PUBLIC SUMMARY

- A scalable gas-phase technology has been developed for the synthesis of MXenes.

- In-depth mechanistic analysis deciphers the origin of the formation of Ti$_2$CCl$_2$.

- Ti$_2$CCl$_2$ MXene has low vacancies and excellent metallic conductivity.

- Ti$_2$CCl$_2$ MXene dramatically prolongs the cyclability of Li-S batteries.

- The strategy pushes MXenes from laboratory to industrial applications.

Gas-phase synthesis of Ti$_2$CCl$_2$ enables an efficient catalyst for lithium-sulfur batteries

Maoqiao Xiang,[1,2] Zihan Shen,[1] Jie Zheng,[1,2] Miao Song,[1,4] Qiya He,[1] Yafeng Yang,[1,2] Jiuyi Zhu,[1] Yuqi Geng,[1,2] Fen Yue,[1,2] Qinghua Dong,[1,2] Yu Ge,[1]
Rui Wang,[1,2] Jiake Wei,[6] Weiliang Wang,[7] Haiming Huang,[8] Huigang Zhang,[1,2,*] Qingshan Zhu,[1,2,3,*] and Chuanfang John Zhang[5]

[1]State Key Laboratory of Multiphase Complex Systems, Institute of Process Engineering, Chinese Academy of Sciences, Beijing 100190, China
[2]School of Chemical Engineering, University of the Chinese Academy of Sciences, Beijing 100049, China
[3]Innovation Academy for Green Manufacture, Chinese Academy of Sciences, Beijing 100190, China
[4]China Nuclear Power Engineering Co., Ltd., 117 West Third Ring Road, North Section, Beijing 100840, China
[5]College of Materials Science & Engineering, Sichuan University, Chengdu 610065, China
[6]State Key Laboratory of Catalysis, Dalian Institute of Chemical Physics, Chinese Academy of Sciences, Dalian 116023, China
[7]School of Physics, Guangdong Province Key Laboratory of Display Material and Technology, Center for Neutron Science and Technology, Sun Yat-sen University, Guangzhou 510275, China
[8]Solid State Physics & Material Research Laboratory, School of Physics and Materials Science, Guangzhou University, Guangzhou 510006, China
*Correspondence: hgzhang@ipe.ac.cn (H.Z.); qszhu@ipe.ac.cn (Q.Z.)
Received: August 19, 2023; Accepted: November 16, 2023; Published Online: November 19, 2023; https://doi.org/10.1016/j.xinn.2023.100540
© 2023 The Authors. This is an open access article under the CC BY-NC-ND license (http://creativecommons.org/licenses/by-nc-nd/4.0/).
Citation: Xiang M., Shen Z., Zheng J., et al., (2024). Gas-phase synthesis of Ti$_2$CCl$_2$ enables an efficient catalyst for lithium-sulfur batteries. The Innovation 5(1), 100540.

MXenes have aroused intensive enthusiasm because of their exotic properties and promising applications. However, to date, they are usually synthesized by etching technologies. Developing synthetic technologies provides more opportunities for innovation and may extend unexplored applications. Here, we report a bottom-up gas-phase synthesis of Cl-terminated MXene (Ti$_2$CCl$_2$). The gas-phase synthesis endows Ti$_2$CCl$_2$ with unique surface chemistry, high phase purity, and excellent metallic conductivity, which can be used to accelerate polysulfide conversion kinetics and dramatically prolong the cyclability of Li-S batteries. In-depth mechanistic analysis deciphers the origin of the formation of Ti$_2$CCl$_2$ and offers a paradigm for tuning MXene chemical vapor deposition. In brief, the gas-phase synthesis transforms the synthesis of MXenes and unlocks the hardly achieved potentials of MXenes.

INTRODUCTION

MXenes, as the frontier of the two-dimensional (2D) materials family,[1−3] have been extensively studied owing to their extraordinary properties[4,5] and promising applications in catalysis,[6,7] photodetection,[8] sensors,[9] electromagnetic interference shielding,[10] hydrogen evolution reaction,[11,12] energy storage,[13−19] and so on. MXenes are usually denoted as M$_{n+1}$X$_n$T$_x$ (n = 1−4), where M represents an early transition metal (e.g., Ti, Zr, Mn, V, Cr, Mo, Ta, Nb, Hf), X is carbon and/or nitrogen, and T stands for surface terminations (such as −O, −F, −OH, −Cl, and −Br; see Figure 1A). Recently, MXenes have aroused extreme enthusiasm in Li-S batteries because of the tremendous potential to inhibit the shuttle effect and suppress the Li dendrites.[20] The Cl-terminated MXenes are expected to be more stable,[13,16,21] exhibit higher electrical conductivity, and exhibit enhanced electrochemical behavior,[22,23] especially for Ti$_2$CCl$_2$ MXene.[24] However, a simple, fast, and low-cost method for scalable synthesis of pure Cl-terminated MXenes still faces great challenges.

At present, the predominant synthesis of MXenes is based on chemical and/or electrochemical etch,[1] in which the A-layer atoms (e.g., Al, Si, P, S, Ga) are selectively removed from the parental MAX phases (M$_{n+1}$AX$_n$).[25,26] As a result, functional groups (T$_x$) subsequently terminate the sites where A atoms are located, enabling the hydrophilic nature of MXenes (Figure 1B). To date, ∼40 different types of MXenes have been successfully synthesized.[26] However, etch technologies require costly MAX precursors; consume a large amount of water, hazardous hydrofluoric acid (HF), or Lewis acidic molten salts; and generate substantial waste.[24,27,28] In addition, the MXenes obtained usually suffer from degradation under air and aqueous solution mainly due to cation vacancies,[29,30] particularly in the case of Ti$_2$CT$_x$.[31−33] Very recently, a direct gas-solid synthetic route was developed to synthesize MXenes using solid Ti foil or powder as titanium source.[27] The gas-solid reaction suffers from mass transfer barrier because the newly formed MXenes covered the Ti source and impeded the further reactions, resulting in long synthesis time and high synthesis temperature. For example, even with an extended synthesis period of 5 days at 950°C, residual raw materials can still be detected in the final product when using Ti, graphite, and TiCl$_4$ as raw materials.[27] In addition, the final product always contained TiC impurity due to the high synthesis temperature. Therefore, a revolution in synthetic technologies is urgently needed.

Here, we break the limitations by inventing a gas-phase synthesis strategy in a fluidized bed reactor (FBR) to produce Ti$_2$CCl$_2$ MXenes without TiC impurity in a large amount (0.1 kg per batch). The synthesis temperature (770°C) is much lower than that previously reported (950°C).[27] We show that a single Ti source can successfully directly synthesize MXenes, which was previously reported to be impossible.[27] Theoretical analyses reveal that subtly tuning the chemical potentials of precursors would lead reactions to the predominance region for the formation of only Ti$_2$CCl$_2$. The FBR synthetic route also enables continuous and scalable production of highly stable MXenes and provides adequate stimuli to push MXenes from laboratories to industry-scale applications.

RESULTS AND DISCUSSION

Synthesis and characterization of Ti$_2$CCl$_2$

Figure 1C schematically illustrates the fluidized bed chemical vapor deposition (CVD) process, in which, homemade solid TiCl$_3$ precursors were transferred into an FBR at 770°C and immediately sublimated to form sufficient gaseous precursors for subsequent nucleation. The gaseous precursors were carried by Ar gas to react with CH$_4$ in the upper FBR region to generate Ti$_2$CCl$_2$ powders (see supplemental material synthesis and Figure 1 for details). Approximately 0.1 kg Ti$_2$CCl$_2$ powders were fabricated per batch (Figure S2), highlighting the high-efficiency features of the FBR strategy.

The X-ray diffraction (XRD) peaks (Figure 2A) of the gas synthesized powder agree well with those of a single hexagonal Ti$_2$CCl$_2$ phase (a = 3.2240 Å and c = 8.6578 Å, P $\overline{3}$ m1 space group). No impurity peaks (e.g., TiC) were observed. Scanning electron microscopy (SEM) analyses reveal hexagonal symmetry flakes (Figures 3 and S1B), suggesting that Ti$_2$CCl$_2$ prefers to grow the morphology as determined by its crystallographic structure. Energy-dispersive X-ray (EDX) spectroscopy (Figure S3) indicates the presence of Ti, C, and Cl (Figure S3). The Cl/Ti atomic ratio was roughly estimated to be 1.02, which was further confirmed by X-ray fluorescence (XRF, Table S1) technology. Raman spectra (Figure S4) display the 2A$_{1g}$ and 2E$_g$ vibration modes of Ti$_2$CCl$_2$, which is confirmed by the density functional theory (DFT) simulation (Figure S5). The X-ray photoelectron spectroscopy (XPS) analysis shows that the Ti 2p signal (Figure S6) contains a tiny portion of Ti-O components (2.56 atom %), which is much lower than the reported MXenes (Table S2). The detection of oxygen is probably due to oxygen contamination during the sample transfer.[34] After Ar ion etching, the Ti$_2$CCl$_2$ and Ti-O content decreases to 1.31 atom % (Figure S7), showing a lower Ti-O content within the material itself.

Cross-sectional SEM observations (Figure 2B) reveal that the as-synthesized Ti$_2$CCl$_2$ flake has multilayer stacking morphology. The atomic force microscopy (AFM) analysis in Figure 2C indicates that the average height of a Ti$_2$CCl$_2$ flake is ∼2.4 nm, corresponding to 2–3 layers per flake. The surface area of Ti$_2$CCl$_2$ (236 m^2 g^{-1}) is ∼2.6 times smaller than that of the theoretical value for single layer Ti$_2$CCl$_2$ (609 m^2 g^{-1}; Figure S8). These multilayer stacking Ti$_2$CCl$_2$ flakes (Figure S9) can be delaminated by n-butyllithium in hexane (Figures S10−S14). A flexible film (Figure S15) was prepared by filtrating the delaminated flake solution under vacuum. Its XRD pattern displays a (0001) peak shift toward lower angles by ∼3.3°, confirming the delamination of Ti$_2$CCl$_2$.
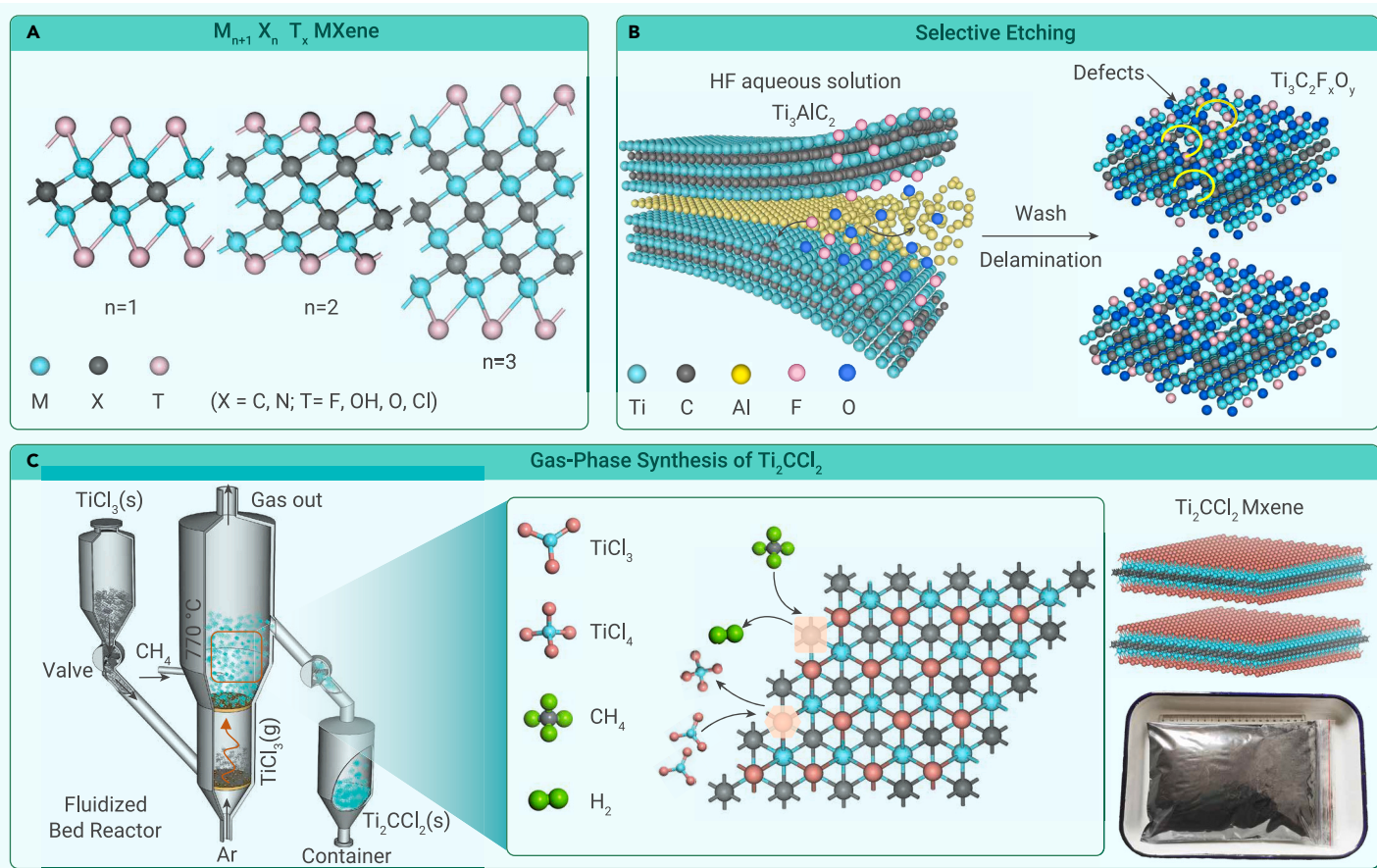
Figure 1. Schematic illustration of $M_{n+1}X_nT_x$ and gas-phase synthesis of Ti_2CCl_2 (A) Schematic crystal structures of $M_{n+1}X_nT_x$ (n = 1, 2, 3). (B) Schematic illustration of the conventional HF etching of Al atomic layers of Ti_3AlC_2 to synthesize $Ti_3C_2T_x$ MXene with defects. Atoms in light blue, light gray, pink, yellow, and blue represent Ti, C, F, Al, and O, respectively. (C) An FBR CVD process is proposed, in which homemade $TiCl_3$ powders were transferred into an FBR and sublimated to form a gaseous $TiCl_3(g)$ precursor and then be carried by Ar to react with $CH_4(g)$ at 770°C to synthesize Ti_2CCl_2 (~0.1 kg Ti_2CCl_2 powders can be fabricated in 5 h).

Furthermore, one flake was observed by an aberration-corrected high-angle annular dark-field (HAADF) scanning transmission electron microscopy (STEM). Figure 2D clearly shows a typical 2D hexagonal lattice of Ti and Cl atoms on the (0001) plane. The side-view HAADF-STEM image of a Ti_2CCl_2 flake displays the typical 2D layer structures with a large interlayer spacing due to van der Waals forces (Figure 2E). Each strip appears to contain four atomic layers, with two Cl layers located on the top surface and two Ti layers in the subsurface (carbon atoms are too light to be imaged well).

To understand the coordination structure, we analyzed the X-ray absorption near-edge structure and extended X-ray absorption fine structure (EXAFS) of the as-synthesized Ti_2CCl_2. The weak pre-edge peak at 4,971 eV and strong absorption edge at 4,986 eV (Figure S16) are attributed to the transition of 1s electrons to the hybridized t_{2g} (Ti 3d + C 2p) and e_g (Ti 3d + C 2p) orbitals and the dipole-allowed transition of 1s electrons to unoccupied Ti 4p states,[35] respectively. The fitting results from the EXAFS curve of Ti_2CCl_2 in Figure 2F show the Ti−C, Ti−Cl, and Ti−Ti scattering paths;[2] the coordination number of Ti−C, Ti−Cl, and Ti−Ti (the nearest neighbor Ti on the opposite side) is determined as 3, 3, and 3, respectively (Figure S17; Table S3). The Ti−C, Ti−Cl, and Ti−Ti scattering paths are also confirmed by the wavelet transform (WT) of the EXAFS spectra in Figure 2G. The electron paramagnetic resonance (EPR) is used to compare the defects in two types of MXenes.[36] As shown in Figure 2H, the etch-derived Ti_2CT_x exhibits a sharp peak at 1.95, which is absent in Ti_2CCl_2. These structural characterizations confirm that the Ti_2CCl_2 powder synthesized by the FBR is Cl terminated and has relatively low vacancies. In addition, the oxidation state of Ti_2CCl_2 (after exposing to air) was analyzed by XPS and compared to etch-derived Ti_2CT_x under the same condition. For Ti_2CT_x, the Ti-O content of Ti 2p signals increases sharply from 21.35 to 38.51 atom % in 24 h (Figure S18). In contrast, that for Ti_2CCl_2 slightly increases from 2.56 to 9.78 atom %. Even after 480 h, the Ti-O content of the Ti_2CCl_2 powder increases to only 14.59 atom % (Figure S19), indicating that the environmental stability of

Ti_2CCl_2 is much higher than that of etch-derived Ti_2CT_x, probably due to lower defects in the as-synthesized Ti_2CCl_2 powder (Figure 2H). In addition, the thermal stability of Ti_2CCl_2 powder was evaluated by calcinating the Ti_2CCl_2 powder at different temperatures under Ar. The results show that Ti_2CCl_2 would partially decompose into TiC at 800°C and completely change into TiC at 850°C (Figure S20). Furthermore, four-probe measurements indicate that Ti_2CCl_2 has a high electric conductivity of 3,257 S m^{-1} (Figure 2I), which is higher than commercial TiC and synthetic Ti_2CT_x obtained by a conventional etching route.

Synthetic mechanism of Ti_2CCl_2

To understand the synthesis mechanism, we calculated the thermodynamic properties of several key compounds involved in the Ti−C−Cl ternary system and analyzed potential conversion reactions among these compounds. The results of calculated cohesive energy (Figure S21) predict that the synthesis of MXene may be readily introduced with TiC impurities or even fail because TiC is the relatively stable phase. Under thermodynamic equilibrium conditions,[37] the formation of Ti_2CCl_2 requires the chemical potentials of constituent elements ($\Delta\mu_i$) to satisfy the following equation:

$$2\Delta\mu_{Ti} + \Delta\mu_C + 2\Delta\mu_{Cl} = \Delta H(Ti_2CCl_2) \qquad \text{(Equation 1)}$$

where $\Delta H(Ti_2CCl_2)$ is the formation energy of Ti_2CCl_2. Toward the upper right of the $\Delta H(Ti_2CCl_2) = -7.19$ eV plane (more negative total chemical potential), Ti_2CCl_2 can be formed spontaneously. To avoid the formation of impurities, the preferred region for Ti_2CCl_2 should exclude the formation of any other species. The shaded area in Figure 3A shows a region where pure Ti_2CCl_2 is formed, indicating that the synthesis of Ti_2CCl_2 in a Ti−C−Cl system is thermodynamically feasible. The calculation offers a tool to tune the chemical potentials of the $TiCl_3/CH_4$ mixture (Figure S22) so that high-purity Ti_2CCl_2 forms thereafter under the optimized CVD conditions without secondary phase.
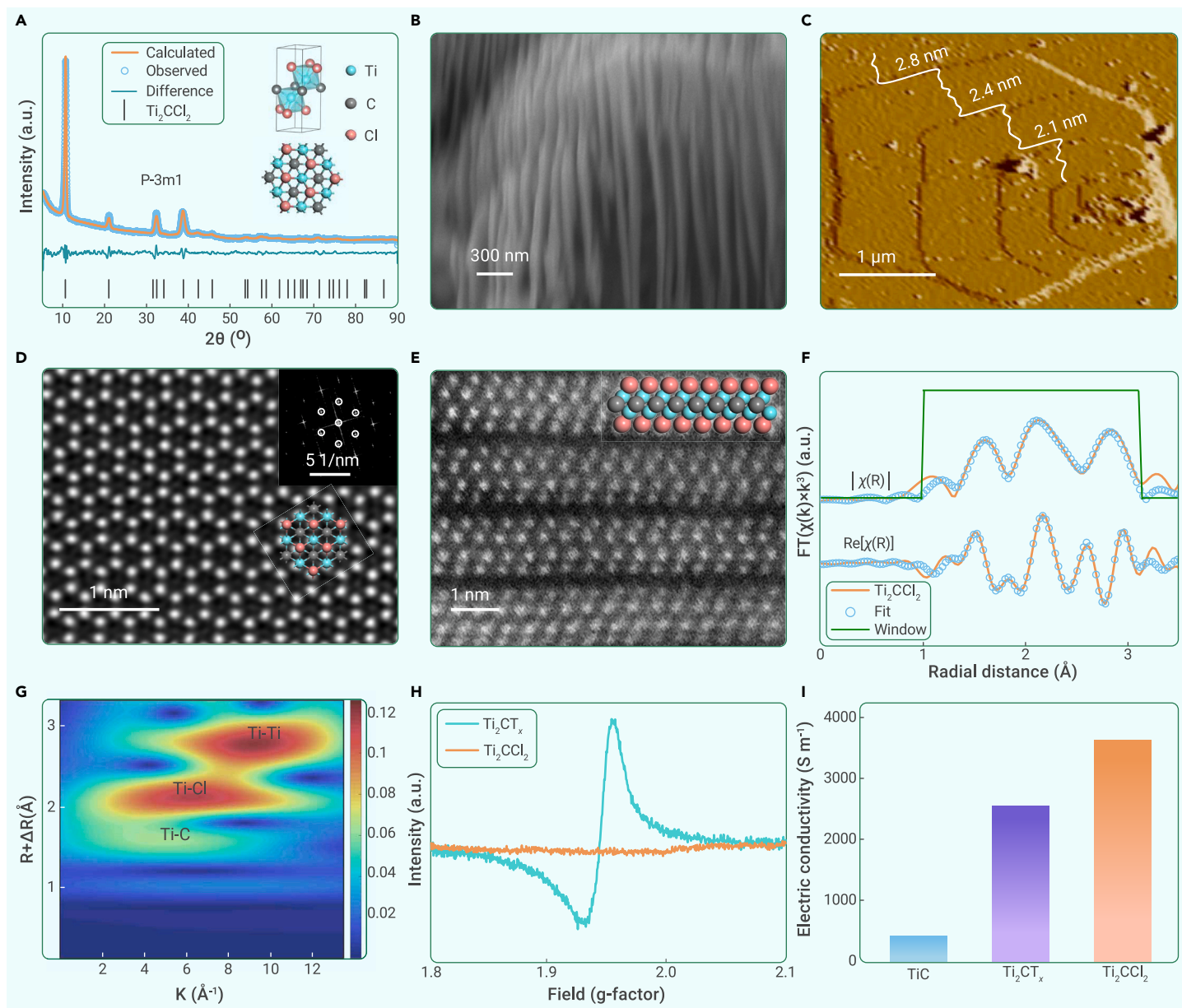
Figure 2. Structural characterization and analysis of Ti₂CCl₂ (A) XRD intensity diagrams of Ti$_2$CCl$_2$ before delamination. The geometric models are the side and top views of the Ti$_2$CCl$_2$ structure. (B) Cross-sectional SEM image of stacked Ti$_2$CCl$_2$ layers. (C) AFM image of a Ti$_2$CCl$_2$ hexagonal flake, showing terraces of different heights. (D and E) Atomically resolved HAADF-STEM images of (D) the (0001) plane of a Ti$_2$CCl$_2$ flake (the inset shows its fast Fourier transform pattern) and (E) its cross-sectional view (the inset shows a correspondingly atomic arrangement). (F) Ti K-edge EXAFS (line) and the curve fit (points) for the as-synthesized Ti$_2$CCl$_2$ without phase correction. (G) WT of the XAS spectra of Ti$_2$CCl$_2$. (H) EPR spectra of Ti$_2$CCl$_2$ (red line) and Ti$_2$CT$_x$ (blue line). (I) The electric conductivity of TiC, Ti$_2$CCl$_2$, and Ti$_2$CT$_x$ pellets.

The precursor selection also heavily influences the product composition. For instance, when using pure substances (Ti, C, and Cl$_2$) as precursors, the solid-solid reaction kinetics is generally slow,[27] leading to the inclusion of impurities due to incomplete conversion. Replacing the solid precursor with gaseous TiCl$_4$ and CH$_4$ lifts the minimum reaction temperature over 1,000°C, producing TiC as the only solid product (Figure S23). However, when TiCl$_3$ and CH$_4$ are used as raw materials, Ti$_2$CCl$_2$ is obtained at a relatively low temperature of 770°C. Increasing the reaction temperature initiates the transformation of Ti$_2$CCl$_2$ to TiC, forming a TiC-Ti$_2$CCl$_2$ binary coexisting system. Above 850°C, only TiC is observed in the final product (Figure 3B). The critical temperature range well explains that the FBR synthesis of Ti$_2$CCl$_2$ is highly temperature dependent. These experimental results also agree with the DFT calculations, implying that the electronic energy, rather than entropy, dominates the Ti$_2$CCl$_2$ formation mechanism.

To further decipher the reaction mechanism, two possible reaction pathways are assumed, according to the mass conservation principle and thermodynamic simulation: (1) 6TiCl$_3$ + CH$_4$ = Ti$_2$CCl$_2$ + 4TiCl$_4$ + 2H$_2$, and (2) 2TiCl$_3$ + CH$_4$ = 2 Ti$_2$CCl$_2$ + 4HCl. Before analyzing the by-products, a cold trap (−30°C) was

used for the removal of possible TiCl$_4$ in the exhaust to prevent the damage of instruments (Figure S24). A subsequent gas chromatographic analysis in Figure 3C reveals that H$_2$ and CH$_4$ were detected, indicating that the formation of Ti$_2$CCl$_2$ follows the first H$_2$ pathway. Figure 3D summarizes the overall reaction pathway from TiCl$_4$ toward Ti$_2$CCl$_2$. TiCl$_4$ does not react with CH$_4$ below 1,000°C. However, Ti$_2$CCl$_2$ decomposes at 850°C. Therefore, TiCl$_4$ and CH$_4$ cannot be used directly to synthesize Ti$_2$CCl$_2$. Once TiCl$_4$ is reduced to metastable TiCl$_3$, the high activity of TiCl$_3$ will lead to the rapid and efficient carbonization of TiCl$_3$ to form Ti$_2$CCl$_2$, with H$_2$ and TiCl$_4$ as by-products.

Catalytic activity of Ti₂CCl₂ in Li-S batteries

The high electronic conductivity and large surface area of Ti$_2$CCl$_2$ inspire us to investigate its potential applications in energy storage. Concurrently, it is noteworthy that within the operational voltage range of Li-S batteries, the Ti$_2$CCl$_2$ catalyst does not exhibit Li self-deintercalation properties (Figure S25). It maintains a nonparticipatory role in Li-S battery electrochemical processes while demonstrating robust structural stability. Ti$_2$CCl$_2$ was added to Li-S batteries and also compared with the widely used additives such as acetylene black (AB), cubic
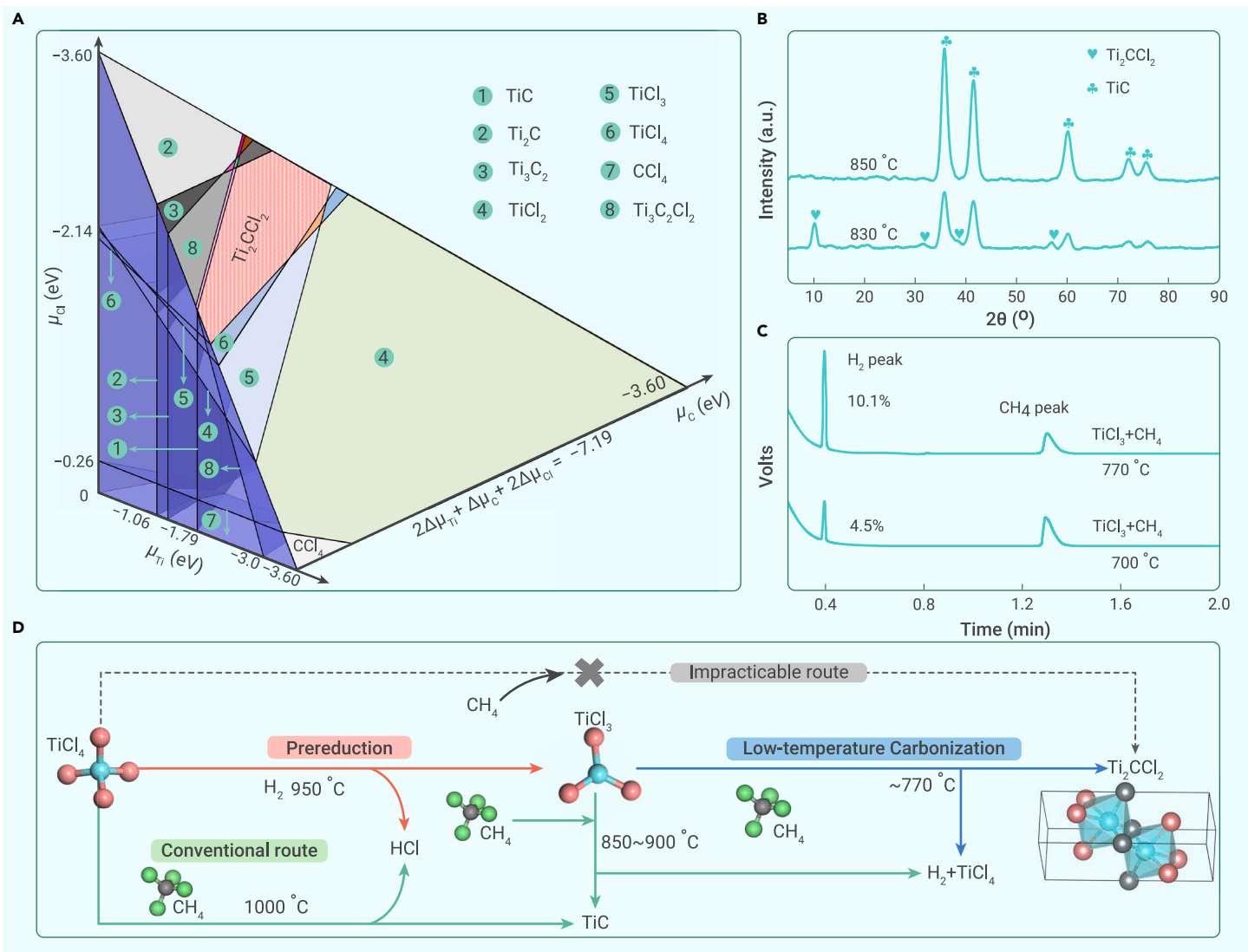
Figure 3. Mechanism of the Ti$_2$CCl$_2$ formation (A) Predominance region of Ti$_2$CCl$_2$ in the coordinate system of $\Delta\mu_{Ti}$, $\Delta\mu_C$, and $\Delta\mu_{Cl}$. (B) XRD patterns of the products synthesized using TiCl$_3$ and CH$_4$ precursors at various temperatures. (C) Gas chromatographs of the exhaust gas using a mixture of TiCl$_3$ and CH$_4$ at different temperatures. (D) Possible reaction routes for the synthesis of Ti$_2$CCl$_2$.

TiC, and Ti$_2$CT$_x$. The thermogravimetric analysis shows that the loading mass of S on Ti$_2$CCl$_2$ MXene is 76 wt % (Figure S26). The loaded S is confirmed by the EDX elemental mapping analysis of S in the S composite (Figure S27). The specific surface area and pore volume decreases from 236 m^2 g^{-1} and 0.6 cm^3 g^{-1} in the Ti$_2$CCl$_2$ MXene to 72 m^2 g^{-1} and 0.2 cm^3 g^{-1} in the S composite (Figure S28) due to the impregnation of S.[38,39] The interaction between S and Ti$_2$CCl$_2$ in the S composite was analyzed by XPS. The S-Ti bond is found in the S composite and in the Li$_2$S$_4$ solution soaked Ti$_2$CCl$_2$ (Figure S29) due to the Lewis acid-base interaction,[39] agreeing with previous report,[39-41] indicating a strong Ti-S interaction.

Figure 4A shows the cyclic voltammetric (CV) curves for three symmetric cells (which use two identical electrodes as the cathode and the anode). Ti$_2$CCl$_2$ delivers a high current and exhibits more well-separated peaks upon either cathodic or anodic scan compared to those of counterpart, implying a more pronounced catalytic effect.[42] By extracting the exponential region of the CV curves, the Tafel slopes of symmetric cells were calculated as shown in Figure 4B. A low Tafel slope for Ti$_2$CCl$_2$ (62 mV dec^{-1}) indicates the enhanced catalytic conversion as compared to those of TiC (102 mV dec^{-1}), AB (186 mV dec^{-1}), and Ti$_2$CT$_x$ (132 mV dec^{-1}; Figure S30). The CV curves in Figure S31 show that the peak currents of Ti$_2$CCl$_2$ increase more rapidly with scan rates than those of TiC, confirming that Ti$_2$CCl$_2$ could accelerate the diffusion of Li ions. In addition, Ti$_2$CCl$_2$ also demonstrates a short semicircle diameter in the Nyquist curves (Figure 4C). Because the diameter is inversely proportional to the reaction rate constants, Ti$_2$CCl$_2$ enhances the conversion of polysulfides.

Figure 4D presents the galvanostatic charge/discharge curves of Li-S batteries containing Ti$_2$CCl$_2$, AB, and TiC in cathodes. Ti$_2$CCl$_2$ requires a much lower half-capacity voltage gap (150 mV) at 0.1 C than TiC (234 mV) and AB (279 mV), implying that the catalytic effect demonstrated in symmetric cells could improve the kinetics of Li-S full cells. Furthermore, the galvanostatic intermittent titration technique (GITT) analysis offers valuable insights into the contrasting charge-transfer rates exhibited by the two cells in a dynamic context, as visually depicted in Figure S32. Notably, during the periods of rest, the Ti$_2$CCl$_2$ cell demonstrates notably diminished voltage drops (attributable to internal resistance) compared to those observed in the TiC cell. This discrepancy indicates a heightened level of chemical diffusion efficiency within the Ti$_2$CCl$_2$ cell. We undertook a meticulous assessment and juxtaposition of the self-discharge characteristics, a crucial endeavor aimed at substantiating the adsorption and catalytic proficiency of the Ti$_2$CCl$_2$ catalyst throughout the dynamic Li-S charging and discharging sequence. Evidently illustrated in Figure S33, we diligently tracked the voltage fluctuations across two distinct cells: one incorporating the Ti$_2$CCl$_2$ catalyst and the other using TiC. This scrutiny extended over a duration of 85 h. Compellingly, the Ti$_2$CCl$_2$ cell demonstrated a notably diminished voltage attenuation compared to its TiC counterpart, thereby signifying its manifestly superior capacity to impede the diffusion of polysulfides. This observation underscores the catalytic prowess of the Ti$_2$CCl$_2$ catalyst in mitigating undesirable polysulfide migration.

In addition, Ti$_2$CCl$_2$ also exhibits excellent rate capabilities (Figure S34) and long-term cyclability (Figure 4E). The capacity of the Ti$_2$CCl$_2$ cell decreases
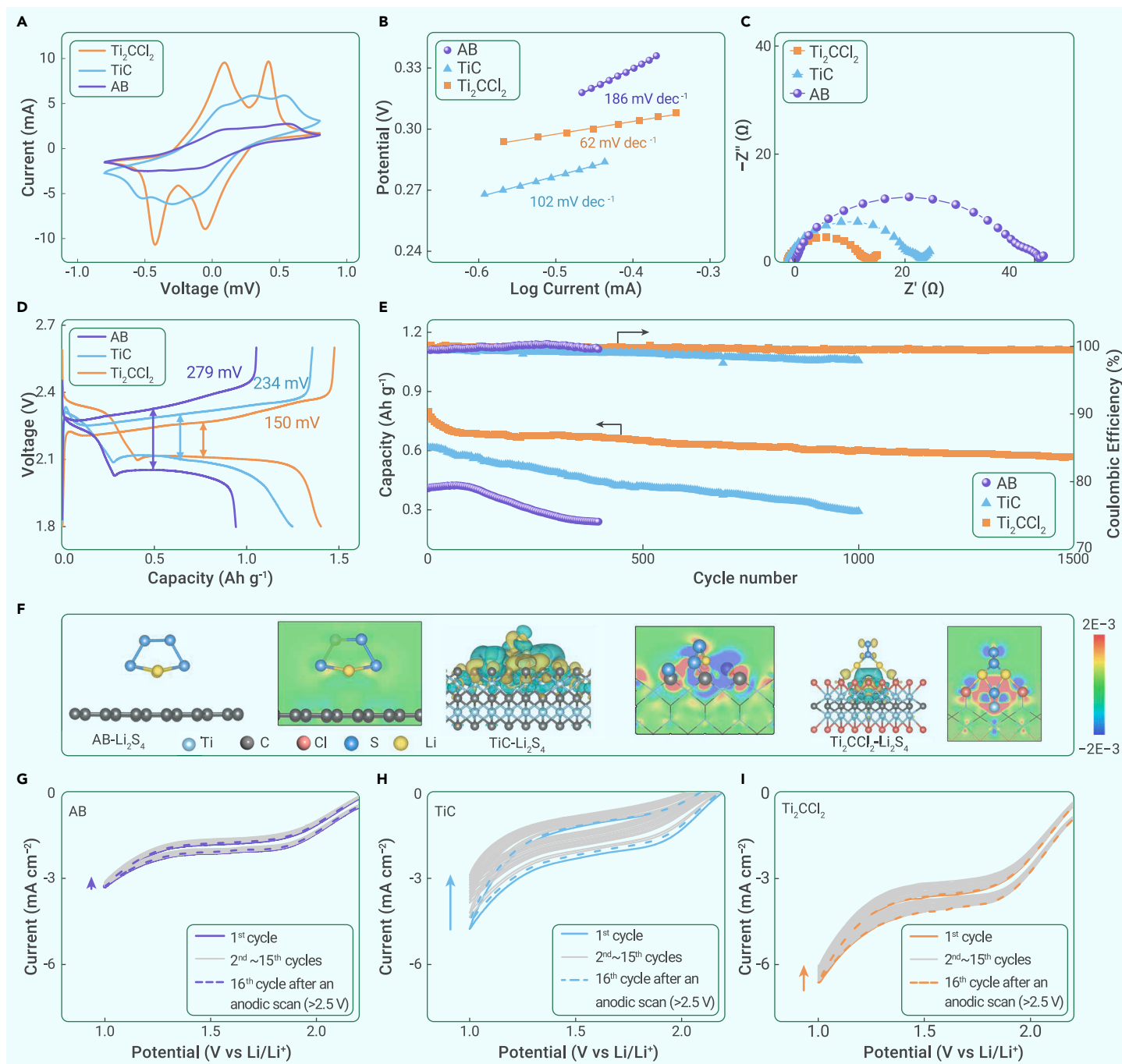
Figure 4. Electrocatalytic properties of Ti₂CCl₂ in Li-S batteries (A and B) CV curves at a scan rate of 7 mV s^{-1} (A), and Tafel plots a comparison of three electrode additives (B). (C) Nyquist plots of the symmetric cells using Ti₂CCl₂, TiC, and AB. (D) Galvanostatic charge/discharge curves at 0.1 C. (E) Cycling properties of Li-S full cells at 2 C. (F) Corresponding geometric configurations and electron density difference diagrams of polysulfides on Ti₂CCl₂, TiC, and AB (where yellow and blue represent the accumulation and reduction of electrons, respectively; isosurface value ±0.002). (G–I) Energy profiles of the reduction of polysulfides on Ti₂CCl₂, TiC, and AB. Polarization curves of (G) AB, (H) TiC, and (I) Ti₂CCl₂ on rotating disk electrodes.

from 800.5 to 569.5 mAh g^{-1} in 1,500 cycles, corresponding to 71% of its initial capacity and a low decay rate of 0.019% per cycle, which dramatically outperforms that of the AB- and TiC-based cells (AB: 58.5% after 400 cycles and TiC: 52.9% after 1,000 cycles). An SEM image of the electrode after the electrochemical test shows that the Ti₂CCl₂ flakes could be well maintained (Figure S35), confirming its highly stability. Specifically, the Ti₂CCl₂ cathode delivers a high initial reversible capacity of 803.7 mAh g^{-1} or 4.02 mAh cm^{-2} under high S loading of 5 mg cm^{-2} (Figure S36). The capacity retention of 65.3% could be achieved after 200 cycles. These results illustrate that the Ti₂CCl₂ cathode can effectively avoid the severe shuttling effect and can accelerate the polysulfide conversion, which further verifies the superiority of the Ti₂CCl₂ catalyst for advanced Li-S batteries. Furthermore, we carried out an additional comparative analysis of the

cathode performances in alignment with the recent literature, a summary of which is presented in Table S4.

To reveal the origin of the rapid kinetics associated with Ti₂CCl₂, we modeled Li₂S₄ adsorption on the surfaces of Ti₂CCl₂, TiC, and AB catalysts. Notably, TiC adsorbs polysulfides more strongly than both Ti₂CCl₂ and AB (Figure S37). Strong adsorption is usually considered to lead to high catalytic activity. However, the experimental results in Figure 4 reveal that Ti₂CCl₂, rather than TiC, has the highest kinetics. To reconcile the contradiction between experimental results and theoretical calculation, we modeled Li₂S₄ adsorption on three primarily exposed surfaces and plotted their electron density difference diagrams in Figure 4F. Li₂S₄ is weakly adsorbed on AB mainly because of their different polarities. In stark contrast, TiC could bind Li₂S₄ so strongly that Li₂S₄ was completely

deformed and all S atoms were attracted to the surface Ti atoms. In other words, a theoretically clean TiC surface is so reactive to capture S atoms of Li_2S_4 that subsequent lithiation/desorption steps may be hindered because of the difficulty in the desorption of products. Ti atoms in Ti_2CCl_2 are coordinated with Cl atoms, which could be dissociated by solvation effects (see Figure S38; Table S5), leaving anion vacancies that attract the terminal S atoms of Li_2S_4. Owing to the co-ordination of Cl ions, the attraction of Li_2S_4 toward Ti_2CCl_2 is finely tuned to an appropriate level so that polysulfide conversion is accelerated without compromising the progress of desorption.

To verify the deduction, we summarized the adsorption energies of polysulfides on three samples and plotted them in the free energy profile (Figure S39) of five consecutive reactions (see supplemental Equations 14–18). TiC enhances the lithiation steps from S_8 to Li_2S_6, owing to the strong interaction with polysulfides. However, such strong interactions turn to impede the last two lithiation steps, leading to the steep increase in free energy. Conversely, Ti_2CCl_2 exhibits a general downhill energy diagram, with a minor increase in the last two steps. From an energy-releasing viewpoint, Ti_2CCl_2 facilitates the polysulfide conversion, thereby demonstrating a high catalytic effect.

To further confirm the adverse effect of strong adsorptions, we loaded Ti_2CCl_2 and TiC on a rotation disk electrode (RDE) and analyzed their polarization curves under forced convection. As shown in Figures 4G–4I, Ti_2CCl_2 induces higher current density than TiC. More important, the repeated cathodic scans of Ti_2CCl_2 barely overlapped, showing similar current densities, whereas those of TiC show a significantly decaying current profile. After 15 cycles, an anodic scan is applied and the following 16th cycle could recover the lost current density, indicating that negative polarization induces too many solid polysulfides that passivate the TiC surface. The passivation-regeneration experiments offer supplementary evidence for the high intrinsic activity of TiC, which consolidates the theoretic analysis in Figure 4F. In brief, strong interaction induces passivation, which prevents TiC from having high apparent activity. However, Ti_2CCl_2 demonstrates appropriate adsorption and the best catalytic activity because of Cl termination.

CONCLUSION

In summary, we propose a gas-phase synthetic route to fabricate stable Ti_2CCl_2 MXene and decipher the synthesis mechanism. By carefully devising the predominance region of the Ti-C-Cl system, we are able to discover and expand the possibility of forming Ti_2CCl_2 while avoiding the formation of the most thermodynamically stable TiC. The bottom-up gas-phase synthesis enables unique surface chemistry, low vacancies, and excellent metallic conductivity. More important, the FBR Ti_2CCl_2 synthesis can be continuously operated and readily scaled up at a large-amount industrialized level. The obtained Ti_2CCl_2 with fascinating properties should unlock some important applications. The gas-phase fluidized technique is general and should be able to synthesize other MXene members, which brings exciting opportunities for the large MXene family toward industrial applications.

MATERIALS AND METHODS
Fabrication of Ti_2CCl_2 MXene

$TiCl_4$ (liquid) was bubbled by H_2 (500 mL min^{-1}) and Ar (300 mL min^{-1}) at room temperature to a quartz tube, which was heated at 950°C.[43,44] Solid $TiCl_3$ powder was obtained by condensing the gaseous $TiCl_3$ at ~400°C in the outlet. We collected 25 g $TiCl_3$ powder and sealed them in a container that was connected to an FBR (Φ3 cm × 50 cm). After the FBR temperature was increased to 770°C, $TiCl_3$ was fed in and sublimated to form a gaseous precursor, which was further lifted to the expansion section (Φ7 cm × 30 cm) of the FBR by flowing Ar gas (500 mL min^{-1}). CH_4 (200 mL min^{-1}) was fed into the expansion section simultaneously to initialize the gas synthesis reaction. After 30 min, the solid Ti_2CCl_2 product was slowly cooled to room temperature (5°C min^{-1}) and sealed with Ar. See the supplemental materials for the details of the raw material purity, suppliers, the fabrication of $TiCl_3$ precursor, the delamination of Ti_2CCl_2, and the fabrication of Ti_2CT_x.

Materials characterization

The XRD patterns were obtained using an X'Pert PRO diffractometer (PANalytical, the Netherlands) using Cu Kα (1.542 Å) radiation as the X-ray source, with 0.016 step size at 40 kV and 40 mA. Microstructure and element analyses were conducted using field emission-SEM (JEOL, JSM-7001F, Japan) with an EDX detector (X-Max, Oxford Instruments, UK). High-resolution TEM and HAADF-STEM images were obtained by using JEM2100PLUS

(JEOL, Japan) and Talos F200X electron microscopes, respectively. The surface area and pore size distribution were measured by an automated gas sorption analyzer (Autosorb-iQ, Quantachrome Instrument, USA). The X-ray absorption spectroscopy (XAS) spectra were collected at the Shanghai Synchrotron Radiation Facility, and details of the experimental conditions and data fitting are shown in Note S1 and Table S2. The EPR spectra of the Ti_2CCl_2 and Ti_2CT_x powders were recorded on an EMXplus spectrometer (Bruker, USA). Elemental quantification was conducted by XRF (Axios Max, PANalytical, the Netherlands), ion chromatography (ECO, Metrohm, Switzerland), and a carbon S analyzer (CS-2800G, NCS, China). The morphology and thickness of delaminated Ti_2CCl_2 flakes were observed using an AFM instrument (Multi Mode 8, Bruker). XPS analyses were conducted on a Shimadzu AXIS SUPRA+ spectrometer (Shimadzu, Japan). The zeta potential of a dilute solution of delaminated Ti_2CCl_2 in N-methylformamide was measured with a zeta potential and particle size analyzer ELSZ-2000ZS (Otsuka Electronics, Japan). Raman spectra were obtained with a high-resolution confocal Raman microscopy (Raman-11, Nanophoton Corporation, Japan). See characterization details in the supplemental methods.

DFT calculations

All DFT calculations were performed using a CASTEP code with the general gradient approximation with the Perdew-Burke-Ernzerhof exchange-correlation function. The energy cutoff for the plane-wave basis was set to 500 eV. For surface adsorption, a vacuum slab of 15 Å was added to simulate the real surface. Details of the cohesive energy calculation, thermodynamic predominant for forming Ti_2CCl_2 calculation, and the interaction relationship between polysulfides and catalysts can be found in Notes S2–S4. The binding energies (E_b) between polysulfides and catalysts were calculated as follows:

$$E_b = E_{total} - E_{sub} - E_{Li_2S_n} \qquad \text{(Equation 2)}$$

where E_{total}, E_{sub}, and $E_{Li_2S_n}$ represent the energy of polysulfides adsorbed on catalysts, catalyst, and polysulfides, respectively.

Electrochemical characterizations

The catalysts and S powders (w/w = 2:8) were mixed and sealed in a glass bottle. After heating at 155°C for 12 h, S composites were obtained. S composites (70%), AB (20%), and polyvinylidene difluoride (10%) were dispersed in 1-methyl-2-pyrrolidinone to form a slurry and then coated on Al foil. The obtained cathode was dried at 60°C overnight. The mass loading of S was controlled to be ~1.5 mg cm^{-2} for regular tests and ~5 mg cm^{-2} for the high-S-loading tests. The electrolyte was 1 M lithium bis (trifluoromethane sulfonimide) and 2% $LiNO_3$ in a 1:1 volume ratio mixture of 1,3-dioxolane and 1,2-dimethoxyethane. Celgard 2300 was used as the separator. For symmetric cells, two identical electrodes were used as working and counter electrodes. Li_2S_4 (20 mg mL^{-1}) was dissolved in the baseline electrolyte, and coin 2032–type cells were assembled with 50 μL electrolyte for each cell. For passivation tests, catalysts (2 mg) and AB (1 mg) were dispersed in a mixture of 500 μL deionized water, 500 μL ethanol, and 17 μL Nafion, which was then ultrasonicated for 1 h. Five microliters of catalyst solution were dropped onto the RDE surface. The modified Li foil and graphite rod were used as the reference and counter electrodes, respectively. The electrolyte was the baseline electrolyte containing 0.01 M Li_2S_4. GITT was used for the charge/discharge cycling of the cell, spanning from the open circuit voltage down to 1.7 V. This protocol was executed at a discharge rate of 0.1 C, punctuated by 20-min discharge intervals and 30-min intervals of rest between each cycle. CV and electrochemical impedance spectroscopy measurements were conducted with a potentiostat (Bio-Logic, France). Li-S batteries were galvanostatically charged and discharged using a Land battery tester.

REFERENCES

1. Mohammadi, A.V., Rosen, J., and Gogotsi, Y. (2021). The world of two-dimensional carbides and nitrides (MXenes). Science **327**, 1165.
2. Kamysbayev, V., Filatov, A.S., Hu, H., Rui, X., Lagunas, F., Wang, D., Klie, R.F., and Talapin, D.V. (2020). Covalent surface modifications and superconductivity of two-dimensional metal carbide MXenes. Science **369**, 979–983.
3. Xia, Y., Mathis, T.S., Zhao, M.-Q., Anasori, B., Dang, A., Zhou, Z., Cho, H., Gogotsi, Y., and Yang, S. (2018). Thickness-independent capacitance of vertically aligned liquid-crystalline MXenes. Nature **557**, 409–412.
4. Zheng, W., Sun, B., Li, D., Gali, S.M., Zhang, H., Fu, S., Di Virgilio, L., Li, Z., Yang, S., Zhou, S., Beljonne, D., Yu, M., Feng, X., Wang, H.I., and Bonn, M. (2022). Band transport by large Fröhlich polarons in MXenes. Nat. Phys. **18**, 544–550.
5. Piatti, E., Arbab, A., Galanti, F., Carey, T., Anzi, L., Spurling, D., Roy, A., Zhussupbekova, A., Patel, K.A., Kim, J.M., Daghero, D., Sordan, R., Nicolosi, V., Gonnelli, R.S., and Torrisi, F. (2021). Charge transport mechanisms in inkjet-printed thin-film transistors based on two-dimensional materials. Nat. Electron. **4**, s893–s905.

6. Zhou, H., Chen, Z., López, A.V., López, E.D., Lam, E., Tsoukalou, A., Willinger, E., Kuznetsov, D.A., Mance, D., Kierzkowska, A., Donat, F., Abdala, P.M., Comas-Vives, A., Copéret, C., Fedorov, A., and Müller, C.R. (2021). Engineering the Cu/Mo₂CTₓ (MXene) interface to drive CO₂ hydrogenation to methanol. Nat. Catal. **4**, 860−871.

7. Li, Z., Xiao, Y., Chowdhury, P.R., Wu, Z., Ma, T., Chen, J.Z., Wan, G., Kim, T.H., Jing, D., He, P., Potdar, P.J., Zhou, L., Zeng, Z., Ruan, X., Miller, J.T., Greeley, J.P., Wu, Y., and Varma, A. (2021). Direct methane activation by atomically thin platinum nanolayers on two-dimensional metal carbides. Nat. Catal. **4**, 882−891.

8. Xu, H., Ren, A., Wu, J., and Wang, Z. (2020). Recent advances in 2D MXenes for photodetection. Adv. Funct. Mater. **30**, 2000907.

9. Deshmukh, K., Kovářík, T., and Khadheer Pasha, S.K. (2020). State of the art recent progress in two dimensional MXenes based gas sensors and biosensors: a comprehensive review. Coord. Chem. Rev. **424**, 213514.

10. Shahzad, F., Alhabeb, M., Hatter, C.B., Anasori, B., Man Hong, S., Koo, C.M., and Gogotsi, Y. (2016). Electromagnetic interference shielding with 2D transition metal carbides (MXenes). Science **353**, 1137−1140.

11. Zhang, J., Zhao, Y., Guo, X., Chen, C., Dong, C.L., Liu, R.S., Han, C.P., Li, Y., Gogotsi, Y., and Wang, G. (2018). Single platinum atoms immobilized on an MXene as an efficient catalyst for the hydrogen evolution reaction. Nat. Catal. **1**, 985−992.

12. Kang, Z., Khan, M.A., Gong, Y., Javed, R., Xu, Y., Ye, D., Zhao, H., and Zhang, J. (2021). Recent progress of MXenes and MXene-based nanomaterials for the electrocatalytic hydrogen evolution reaction. J. Mater. Chem. A **9**, 6089−6108.

13. Ghidiu, M., Lukatskaya, M.R., Zhao, M.Q., et al. (2014). Conductive two-dimensional titanium carbide 'clay' with high volumetric capacitance. Nature **516**, 78−81.

14. Li, Y., Shao, H., Lin, Z., Lu, J., Liu, L., Duployer, B., Persson, P.O.Å., Eklund, P., Hultman, L., Li, M., Chen, K., Zha, X.H., Du, S., Rozier, P., Chai, Z., Raymundo-Piñero, E., Taberna, P.L., Simon, P., and Huang, Q. (2020). A general Lewis acidic etching route for preparing MXenes with enhanced electrochemical performance in non-aqueous electrolyte. Nat. Mater. **19**, 894−899.

15. Agresti, A., Pazniak, A., Pescetelli, S., Di Vito, A., Rossi, D., Pecchia, A., Auf der Maur, M., Liedl, A., Larciprete, R., Kuznetsov, D.V., Saranin, D., and Di Carlo, A. (2019). Titanium-carbide MXenes for work function and interface engineering in perovskite solar cells. Nat. Mater. **18**, 1228−1234.

16. Anasori, B., Lukatskaya, M.R., and Gogotsi, Y. (2017). 2D metal carbides and nitrides (MXenes) for energy storage. Nat. Rev. Mater. **2**, 16098.

17. Ming, F., Liang, H., Huang, G., Bayhan, Z., and Alshareef, H.N. (2021). MXenes for rechargeable batteries beyond the lithium-ion. Adv. Mater. **33**, 2004039.

18. Wei, C., Tao, Y., An, Y., Tian, Y., Zhang, Y., Feng, J., and Qian, Y. (2020). Recent advances of emerging 2D MXene for stable and dendrite-free metal anodes. Adv. Funct. Mater. **30**, 2004613.

19. Li, M., Li, X., Qin, G., Luo, K., Lu, J., Li, Y., Liang, G., Huang, Z., Zhou, J., Hultman, L., Eklund, P., Persson, P.O.Å., Du, S., Chai, Z., Zhi, C., and Huang, Q. (2021). Halogenated Ti₃C₂ MXenes with electrochemically active terminals for high performance Zinc ion batteries. ACS Nano **15**, 1077−1085.

20. Zhao, Q., Zhu, Q., Liu, Y., and Xu, B. (2021). Status and prospects of MXene-based lithium−sulfur batteries. Adv. Funct. Mater. **31**, 2100457.

21. Li, M., Lu, J., Luo, K., Li, Y., Chang, K., Chen, K., Zhou, J., Rosen, J., Hultman, L., Eklund, P., Persson, P.O.Å., Du, S., Chai, Z., Huang, Z., and Huang, Q. (2019). Element replacement approach by reaction with lewis acidic molten salts to synthesize nanolaminated MAX phases and MXenes. J. Am. Chem. Soc. **141**, 4730−4737.

22. Sun, W., Shah, S.A., and Green, M.J. (2017). Electrochemical etching of Ti₂AlC to Ti₂CTₓ (MXene) in low-concentration hydrochloric acid solution. J. Mater. Chem. A **5**, 21663−21668.

23. Kajiyama, S., Szabova, L., Iinuma, H., Sugahara, A., Gotoh, K., Sodeyama, K., Tateyama, Y., Okubo, M., and Yamada, A. (2017). Enhanced Li ion accessibility in MXene titanium carbide by steric chloride termination. Adv. Energy Mater. **7**, 1601873.

24. Ma, G., Shao, H., Xu, J., Liu, Y., Huang, Q., Taberna, P.L., Simon, P., and Lin, Z. (2021). Li-ion storage properties of two-dimensional titanium-carbide synthesized via fast one-pot method in air atmosphere. Nat. Commun. **12**, 5085.

25. Wei, Y., Zhang, P., Soomro, R.A., Zhu, Q., and Xu, B. (2021). Advances in the synthesis of 2D MXenes. Adv. Mater. **33**, 2103148.

26. Shuck, C.E., and Gogotsi, Y. (2020). Taking MXenes from the lab to commercial products. Chem. Eng. J. **401**, 125786.

27. Wang, D., Zhou, C., Filatov, A.S., Cho, W., Lagunas, F., Wang, M., Vaikuntanathan, S., Liu, C., Klie, R.F., and Talapin, D.V. (2023). Direct synthesis and chemical vapor deposition of 2D carbide and nitride MXenes. Science **379**, 1242−1247.

28. Shen, M., Jiang, W., Liang, K., Zhao, S., Tang, R., Zhang, L., and Wang, J.Q. (2021). One-pot green process to synthesize MXene with controllable surface terminations using molten salts. Angew. Chem. Int. Ed. **60**, 27013−27018.

29. Xia, F., Lao, J., Yu, R., Sang, X., Luo, J., Li, Y., and Wu, J. (2019). Ambient oxidation of Ti₃C₂ MXene initialized by atomic defects. Nanoscale **11**, 23330−23337.

30. Sang, X., Xie, Y., Lin, M.W., et al. (2016). Atomic defects in monolayer titanium carbide (Ti₃C₂Tₓ) MXene. ACS Nano **10**, 9193−9200.

31. Bhat, A., Anwer, S., Bhat, K.S., et al. (2021). Prospects challenges and stability of 2D MXenes for clean energy conversion and storage applications. NPJ 2D Mater. Appl. **5**, 61.

32. Iqbal, A., Hong, J., Ko, T.Y., and Koo, C.M. (2021). Improving oxidation stability of 2D MXenes: synthesis, storage media, and conditions. Nano Converg. **8**, 9.

33. Zhang, C.J., Pinilla, S., McEvoy, N., Cullen, C.P., Anasori, B., Long, E., Park, S.H., Seral-Ascaso, A., Shmeliov, A., Krishnan, D., Morant, C., Liu, X., Duesberg, G.S., Gogotsi, Y., and Nicolosi, V. (2017). Oxidation stability of colloidal two-dimensional titanium carbides (MXenes). Chem. Mater. **29**, 4848−4856.

34. Lu, Y., Li, D., and Liu, F. (2022). Characterizing the chemical structure of Ti₃C₂Tₓ MXene by angle-resolved XPS combined with argon ion etching. Materials **15**, 307.

35. Lukatskaya, M.R., Bak, S.-M., Yu, X., Yang, X., Barsoum, M.W., and Gogotsi, Y. (2015). Probing the mechanism of high capacitance in 2D titanium carbide using *in situ* X-ray absorption spectroscopy. Adv. Energy Mater. **5**, 1500589.

36. Ivanovskaya, M., Ovodok, E., Kotsikau, D., Azarko, I., Micusik, M., Omastova, M., and Golovanov, V. (2020). Structural transformation and nature of defects in titanium carbide treated in different redox atmospheres. RSC Adv. **10**, 25602−25608.

37. Buckeridge, J., Scanlon, D.O., Walsh, A., et al. (2014). Automated procedure to determine the thermodynamic stability of a material and the range of chemical potentials necessary for its formation relative to competing phases and compounds. Comput. Phys. Commun. **185**, 330−338.

38. Tang, H., Li, W., Pan, L., Tu, K., Du, F., Qiu, T., Yang, J., Cullen, C.P., McEvoy, N., and Zhang, C.J. (2019). A robust, freestanding MXene-sulfur conductive paper for long-lifetime Li−S batteries. Adv. Funct. Mater. **29**, 19019.

39. Liang, X., Rangom, Y., Kwok, C.Y., Pang, Q., and Nazar, L.F. (2017). Interwoven MXene nanosheet/carbon-nanotube composites as Li−S cathode hosts. Adv. Mater. **29**, 1603040.

40. Liang, X., Garsuch, A., and Nazar, L.F. (2015). Sulfur cathodes based on conductive MXene nanosheets for high performance lithium−sulfur batteries. Angew. Chem. **127**, 3979−3983.

41. Tang, H., Li, W., Pan, L., Cullen, C.P., Liu, Y., Pakdel, A., Long, D., Yang, J., McEvoy, N., Duesberg, G.S., Nicolosi, V., and Zhang, C.J. (2018). In situ formed protective barrier enabled by sulfur@titanium carbide (MXene) ink for achieving high-capacity, long lifetime Li-S batteries. Adv. Sci. **5**, 1800502.

42. Shen, Z., Zhou, Q., Yu, H., Tian, J., Shi, M., Hu, C., and Zhang, H. (2021). CoSe₂/MoS₂ heterostructures to couple polysulfide adsorption and catalysis in lithium-sulfur batteries. Chin. J. Chem. **39**, 1138−1144.

43. Song, M., Yang, Y., Xiang, M., Zhu, Q., and Zhao, H. (2021). Synthesis of nano-sized TiC powders by designing chemical vapor deposition system in a fluidized bed reactor. Powder Technol. **380**, 256−264.

44. Song, M., Chen, D., Yang, Y., Xiang, M., Zhu, Q., Zhao, H., Ward, L., and Chen, X. (2021). Crystal facet engineering of single-crystalline TiC nanocubes for improved hydrogen evolution reaction. Adv. Funct. Mater. **31**, 2008028.

ACKNOWLEDGMENTS

AUTHOR CONTRIBUTIONS

Conceptualization: Q.Z. Methodology: Q.Z. and M.X. Investigation & experiments: M.X., Z.S., J.Z., Q.H., M.S., F.Y., and Q.D. Investigation & calculations: H.Z., Z.S., and M.X. Writing − original draft: M.X., Y.Y., and H.Z. Writing − review & editing: C.J.Z., H.Z., and Q.Z. TEM test & analysis: J.W. DFT simulation of the Raman spectra: W.W. and H.H. All of the authors were involved in the analysis of the data and discussions of the paper.

DECLARATION OF INTERESTS

SUPPLEMENTAL INFORMATION

LEAD CONTACT WEBSITE

http://www.mpcs.cn/ktz/rmce/.